# Deformation profile and interface-mediated defect interaction in Cu/CuZr nanolaminates: An effective-temperature description

Michael Y. Tong, Charles K. C. Lieou, and Irene J. Beyerlein

Phys. Rev. Materials **3**, 073602 — Published 16 July 2019

DOI: 10.1103/PhysRevMaterials.3.073602

# Deformation profile and interface-mediated defect interaction in Cu/CuZr nanolaminates: an effective-temperature description

Michael Tong,[1,2] Charles Lieou,[2,3] and Irene Beyerlein[4]

[1] *Department of Physics, University of California Santa Barbara, Santa Barbara, California 93116, United States of America*
[2] *Center for Nonlinear Studies, Los Alamos National Laboratory, Los Alamos, NM 87545, United States of America*
[3] *Theoretical Division, Los Alamos National Laboratory, Los Alamos, NM 87545, United States of America*
[4] *Department of Mechanical Engineering, Materials Department, University of California, Santa Barbara, CA 93106, United States of America*

(Dated: June 14, 2019)

Both simulations and experiments have suggested that Cu/CuZr nanolaminates are stronger and more ductile than their individual constituents due to interface-mediated interactions between plasticity carriers. In this work, we use the effective-temperature theories of dislocation and amorphous shear-transformation-zone (STZ) plasticity to study amorphous-crystalline interface (ACI) interface-mediated plasticity in Cu/CuZr nanolaminates under mechanical straining. The model is shown to capture reasonably well the measured deformation response when strained either in tension parallel to or in compression normal to the amorphous-crystalline interface. Our analysis indicates that increasing CuZr or decreasing Cu layer thickness increases the maximum flow stress for both perpendicular and parallel loading cases. For the cases of parallel and perpendicular loading, the maximum flow stress values are 3.4 GPa and 2.5 GPa, respectively. Furthermore, increasing the strain rate for the parallel loading case decreases the slip strain in the amorphous and crystalline layers. For the perpendicular loading case, an increase in strain rate decreases the amorphous layer slip but increases the crystalline layer slip. In all slip strain analyses, maximum slip strain occurs at the ACI, thus indicating that plasticity carriers accumulate at the interface and are absorbed there. These findings indicate a significant anisotropy in strength with greater sensitivity to layer thickness for the case of tensile loading parallel to the ACI. Further findings signify that slip strain is more sensitive when the nanolaminate is compressed perpendicular to the ACI.

PACS numbers: 1234

## I. INTRODUCTION

Amorphous/crystalline nanolaminates are drawing the attention of many scientific studies, defense industries, and aerospace industries due to an attractive combination of both high strength and toughness[1–7]. As a novel material, questions still remain regarding the appropriate choice of microstructural features, such as layer thicknesses, and their effect on strength, as well as on the anisotropy of strength. This work aims to better define the space of microstructural parameters leading to high strength and low anisotropy.

There have been several experimental studies on amorphous-crystalline nanolaminates – mostly Cu/CuZr or Zr/CuZr – in which the nanolaminate composite is either subjected to uniaxial tensile loading parallel to the amorphous-crystalline interfaces (ACIs)[4,6], or uniaxial compression or nanoindentation perpendicular to the interfaces[7–9]. In most experimental studies, amorphous/crystalline nanolaminates are made via deposition methods, thereby producing a thin film, and then tested in either tension (in the plane of the film) or compression normal to the layers. While inexpensive to make and amenable to scientific study, such thin film samples are too small for making practical sized structures and this method is not feasibly scalable. Very recently, a group demonstrated the ability to apply the metal forming technique, accumulative roll bonding, to form bulk-sized amorphous/crystalline nanolaminates with layer spacings less than 40 nm[10]. Thus far, these studies reveal the inhibition of shear band formation and propagation in the amorphous glass due to the presence of the nanocrystalline layers, and in some cases homogeneous deformation in the amorphous material[4]. These observations depend, in turn, on the thickness of the amorphous and nanocrystalline layers. These findings suggest that the layered architecture, and in particular the interface, may provide the novel physics that is crucial in accounting for the exceptional strength and ductility of these materials.

In order to shed light on the mechanisms of failure and the role of the interface in deformation, a number of researchers have employed molecular dynamics (MD) simulations. The use of MD simulations to study STZ and dislocation plasticity has become feasible thanks to the advent in computing power over the past decade, enabling a revelation of microstructural changes not accessible by experiments. The seminal work by Wang et al.[4] and a subsequent study by Arman et al.[5] revealed a cooperative slip transfer mechanism, whereby the interface between the nanocrystalline and amorphous layers emits STZs that move into the amorphous layer, upon absorbing dislocations arriving from the crystalline side. Recent

systematic studies conducted by Cheng and Trelewicz[2,3] further confirmed this phenomenon. These authors investigated the effect of different layer thicknesses for both amorphous and nanocrystalline layers on the response of the material under tensile strain parallel to the interface at a constant strain rate, and found that the amorphous-to-crystalline thickness ratio is the primary factor that controls the flow stress. In addition, they quantified the contributions of the amorphous and crystalline materials to the overall plastic response, and noted that most of the slip resides in the portion of the amorphous material immediately adjacent to the amorphous-crystalline interface. They concluded that the layered configuration impedes shear band localization, thereby accounting for the increased toughness of the composite material.

In prior modeling work[1], we applied the effective-temperature concept to study the effect of layer size on the deformation response under tension parallel to the interface. The effective (or fictive) temperature, based upon nonequilibrium thermodynamics, quantifies the configurational disorder in a material, thus providing a systematic, mesoscopic description of the evolution of its microstructural state under external work and, specifically, the evolution of defect densities, which feed back into the mechanical response of the composite to external loads. Our earlier work was based on macroscale property measurements reported in[6]. Recent MD simulation results reported in[2,3], in contrast, offer insight into the heterogeneity of slip strain at different positions throughout the deforming sample. This microscopic information, inaccessible in laboratory experiments, reveals important physics that underlie the interfacial strength between the amorphous and crystalline layers and provides constraints to several model parameters.

In this work, we refine the prior model to calculate the strain distribution across the layers in amorphous-crystalline nanolaminates and use it to investigate the effects of individual amorphous and crystalline layer sizes and the amorphous-to-crystalline layer thickness ratio on the deformation response of a Cu-CuZr nanolaminate. We further vary the loading orientation and strain rates within the range of $10^{-3}$ $s^{-1}$ to $10^{8}$ $s^{-1}$, in order to extrapolate findings in the MD simulations to realistic loading rates not accessible by simulations alone. As in previous work[1], we incorporate into the effective temperature evolution equations a conduction term to describe the interaction between STZs in the amorphous layers and dislocations in the crystalline layers, and to account for the flow of configurational disorder during deformation. Our assumptions of reduced material strength near the interface, motivated by MD simulations, results in increased STZ activity and a significantly increased slip strain in the amorphous layer near the interface, compared to the interior of the amorphous layer, in agreement with simulations. These observations can only be explained in terms of the motion of plasticity carriers (STZs and dislocations), and cannot be captured by macroscopic models alone – hence the need for our present multiscale approach which provides a mesoscale, thermodynamically consistent representation of STZ and dislocation densities.

Through these calculations, we find that the stress-strain behavior of the Cu-CuZr nanolaminate depends primarily on the amorphous-to-crystalline thickness ratio, and only very slightly on the actual thicknesses of the two constituent materials for a given thickness ratio. Specifically, increasing the amorphous-to-crystalline thickness ratio increases the flow stress and generally increases the peak stress under tensile loading parallel to the interfaces and uniaxial compression perpendicular to the interfaces. However, the absolute layer thickness of the two layers considerably alters the slip strain distribution across the interface. In addition, maximum slip strain occurs in the amorphous CuZr adjacent to the Cu/CuZr interface, for both tensile loading parallel to the interfaces, and at slow strain rates for compression loading perpendicular to the interfaces. For compression at fast loading rates almost all of the deformation is in the crystalline Cu. This shift of maximum slip strain from CuZr to Cu as the loading rate increases occurs in the compression loading case for slower strain rates compared to the tensile loading case.

This paper is structured as follows. Since the formulation builds on the effective-temperature theory of plasticity, we begin in Sec. II with a brief review of the effective temperature, and demonstrate how it can be used to describe STZs and dislocations. Next, in Sec. III, we turn our attention to the amorphous-crystalline nanolaminate material, and specialize to the cases of loading parallel and perpendicular to the interfaces. In Sec. IV we present the effects of phase thickness ratio and strain rate. We conclude this paper Sec. V with a discussion of the implications of our findings for the microstructural design of composites for practical applications.

## II. METHODS

In this section we review the effective-temperature theories of dislocation and STZ plasticity, which provide a means to quantify the influence of plasticity carriers on material deformation. We will show how a thermodynamically-defined effective temperature controls the defect densities in the amorphous and crystalline layers, and facilitates a description of defect interaction and flow of disorder across the ACI.

### A. Effective temperature

We begin by introducing the notion of the effective temperature. Interested readers may consult[11] for further details.

The effective temperature provides a tool to describe configurational disorder as well as flow of disorder across

the material. Defects such as dislocations in the crystalline layer and Shear Transformation Zones (STZs) in the amorphous layer are manifestations of configurational disorder. The effective temperature is defined as

$$\chi = \left(\frac{\partial U_C}{\partial S_C}\right), \tag{1}$$

where $U_C$ and $S_C$ are the configurational energy and entropy, respectively, of the material. Here, we use units such that the entropy is dimensionless and the energy and temperature share the same units, in effect setting the Boltzmann constant equal to unity. Thus $[S] = [k_B]\ln(w)$ and $[E] = [k_B][T]$, where $w$ is the number of microstates.

The need for an effective-temperature (or fictive-temperature) description arises from the fact that a deforming material is out of equilibrium by definition; mechanical force drive the configurational degrees of freedom, which include the positions of atoms and therefore defect densities, out of equilibrium with the kinetic-vibrational degrees of freedom. The latter set of degrees of freedom of the material are described by the thermal temperature, while the former, which evolve on a substantially slower time scale than thermal motion, are described by the effective temperature, which may not be equal to the thermal temperature. (See[11] for a technical discussion of this point.) When undergoing deformation, the system dynamically minimizes its configurational free energy

$$F_C = U_C - \chi S_C, \tag{2}$$

so that the accumulated strain steady-state defect densities $\{\rho_\alpha^{ss}\}$ is given by

$$\rho_\alpha^{ss} \propto e^{-e_\alpha/\chi}, \tag{3}$$

where $e_\alpha$ is the formation energy of a single defect of type $\alpha$. Thus, for dislocations with formation energy $e_D$, the steady-state dislocation density is given by

$$\rho^{ss} \propto e^{-e_D/\chi}. \tag{4}$$

The steady-state STZ density takes on a similar form. In addition, STZs can be classified into two states depending on the likelihood of atomic rearrangement for a given deviatoric stress configuration; reversing the deviatoric stress returns an STZ which has just undergone rearrangement to its prior configuration. Thus, these two states give rise to a prefactor of two for the steady-state STZ density[1]:

$$\Lambda^{ss} = 2e^{-e_Z/\chi}, \tag{5}$$

with $e_Z$ being the characteristic STZ formation energy.

The evolution equation for the effective temperature is given by the first law of thermodynamics[11]:

$$c^{\text{eff}}\dot{\chi} = \sigma\dot{\epsilon}^{pl}\left(1 - \frac{\chi}{\chi_0}\right). \tag{6}$$

Here, $c^{\text{eff}}$ is the effective specific heat capacity and $\chi_0$ is the steady-state effective temperature. In what follows, the effective temperature concept will be used to describe plasticity and the kinetics of STZs and dislocations.

### B. STZ plasticity in amorphous solids

Here we provide a brief overview of the shear transformation zone theory, as discussed in[11–13] in greater detail.

At room temperature, below the glass transition[4,6,11–13], STZs fluctuate into and out of existence solely by mechanical work. Plasticity in the amorphous material is associated with the non-affine rearrangement of atoms at STZs, and the plastic strain rate is given by

$$\tau\dot{\gamma}_{ij}^{pl} = \epsilon_0 C(\overline{s})\Lambda\frac{s_{ij}}{\overline{s}}(T(\overline{s}) - m). \tag{7}$$

Here, $m$ denotes the orientational bias, defined as the difference between the densities of the STZs in the two states, divided by the total STZ density. The quantity $s_{ij}$ is the deviatoric stress tensor, related to the Cauchy stress tensor by $s_{ij} = \sigma_{ij} - \frac{1}{3}\text{tr}(\sigma_{ij})$. The stress invariant is $\overline{s} \equiv \sqrt{\frac{1}{2}s_{ij}s_{ij}}$. For the case of uniaxial deformation in the $x$-direction, $s_{xx} = \frac{2}{3}\sigma$ and $s_{yy} = s_{zz} = -\frac{1}{3}\sigma$, where $\sigma$ is the tensile stress, and $\sigma = \sqrt{3}\overline{s}$. Also, $\tau$ is the atomic time scale, $\epsilon_0$ is the ratio of STZ plastic core volume to atomic volume, and $C(\overline{s})$ and $T(\overline{s})$ are combinations of the forward and backward STZ transitions rates $R(\pm\overline{s})$:

$$C(\overline{s}) \equiv \frac{1}{2}(R(\overline{s}) + R(-\overline{s})), \tag{8}$$

and

$$T(\overline{s}) \equiv \frac{R(\overline{s}) - R(-\overline{s})}{R(\overline{s}) + R(-\overline{s})}. \tag{9}$$

Assuming plastic incompressibility, the only nonzero components of the plastic strain rate tensor are

$$\dot{\gamma}_{xx}^{pl} = \dot{\epsilon}^{pl};\ \dot{\gamma}_{yy}^{pl} = \dot{\gamma}_{zz}^{pl} = -\frac{1}{2}\dot{\epsilon}^{pl}, \tag{10}$$

with $\dot{\epsilon}^{pl}$ being scalar version the plastic strain rate.

The tensile or compressive stress $\sigma$ evolves according to Hooke's law:

$$\dot{\sigma}_a = E_a(\dot{\epsilon}_a - \dot{\epsilon}_a^{pl}), \tag{11}$$

where $E_a$ is the Young's modulus and the subscript "$a$" indicates reference to the amorphous material. With equation (10), equation (7) becomes

$$\tau\dot{\epsilon}_a^{pl} = \frac{2}{\sqrt{3}}\epsilon_0\Lambda C(\sigma_a)(T(\sigma_a) - m), \tag{12}$$

where we use, for simplicity, $C(\sigma_a) \equiv C(\overline{s})$ and $T(\sigma_a) \equiv T(\overline{s})$. Based on constraints associated with the second law of thermodynamics, we choose the forward and backward STZ transition rate functions[4,6] to be

$$C(\sigma_a) = \cosh\left(\frac{\epsilon_0\sigma_a a^3}{\sqrt{3}\chi}\right), \tag{13}$$

and

$$T(\sigma_a) = \tanh\left(\frac{\epsilon_0\sigma_a a^3}{\sqrt{3}\chi}\right), \tag{14}$$

where $a$ is the atomic radius.

According to[11] there is a direct proportionality between the heat dissipation per STZ and the mechanical noise strength $\Gamma$, or the rate at which STZs are created and annihilated

$$\Gamma = \frac{\sqrt{3}\tau\sigma_a\dot{\epsilon}_a^{pl}}{\epsilon_0\sigma_0\Lambda}. \tag{15}$$

Direct computation of the steady-state value of the orientational bias[13] gives

$$m = \begin{cases} T(\sigma_a), & \sigma_a T(\sigma_a) \le \sigma_0; \\ \sigma_0/\sigma_a, & \sigma_a T(\sigma_a) > \sigma_0. \end{cases} \tag{16}$$

Thus, $\sigma_0$ emerges as the parameter that controls the yield stress parameter. It originates from the relationship between the plastic dissipation per STZ and mechanical noise strength $\Gamma$.

The equations described in this subsection, as well as equations (6) and (11), completely describe the mechanical response of the amorphous material.

### C. Dislocation plasticity in crystalline solids

In this subsection, we briefly review the effective-temperature description of the kinetics of dislocations[14]. Many parallels can be seen with the STZ theory outlined in the prior section, making it a convenient and consistent framework for modeling the plasticity of a/c composites.

The stress evolves according to Hooke's law:

$$\dot{\sigma}_c = E_c(\dot{\epsilon}_c - \dot{\epsilon}_c^{pl}), \tag{17}$$

where the subscript "$c$" now refers to the crystalline material.

To find $\dot{\epsilon}_c^{pl}$, we start with the Orowan equation. The plastic strain rate, in the case of simple shear, is given by

$$\dot{\gamma}^{pl} = \rho b v, \tag{18}$$

where $\rho$ is now the scalar areal density of mobile dislocations, $b$ is the Burgers vector value, and $v = l/\tau_P(s)$ is the average speed of the dislocations. $l = 1/\sqrt{\rho}$ is the average dislocation spacing and $1/\tau_P(s)$ is the rate that dislocations jump between pinning sites. This mechanism motivates definition of a depinning rate with a stress-dependent energy barrier, i.e.,

$$U_P(s) = k_B T_p e^{-s/\sigma_T}, \tag{19}$$

with $s$ being a scalar value shear stress and $\sigma_T$ being the Taylor depinning stress, which takes the form

$$\sigma_T = \mu_T b\sqrt{\rho}, \tag{20}$$

where $\mu_T$ is the effective shear modulus, which is about 1/30 times the shear modulus $\mu$. Then it follows that the depinning rate is given by

$$\frac{1}{\tau_P(s)} = \frac{1}{\tau} f_p(s), \tag{21}$$

with

$$f_p(s) = \exp(-\frac{T_P}{T}e^{-s/\sigma_T}). \tag{22}$$

The tensorial generalization for the deviatoric plastic strain rate is

$$\dot{\gamma}_{ij}^{pl} = \frac{b\sqrt{\rho}}{\tau}\frac{s_{ij}}{\overline{s}} f_p(\overline{s}). \tag{23}$$

Converting from simple shear to uniaxial tensile or compressive stress, we replace the stress $s$ in the exponential by a scalar stress $\sigma$. Then, along the lines of the arguments presented above for tensile or compressive deformation in the amorphous solid, it follows that

$$\dot{\epsilon}_c^{pl} = \frac{\rho}{2}\frac{2\sigma_c/3}{\sigma_c/\sqrt{3}} v = \frac{1}{\sqrt{3}}\rho b v, \tag{24}$$

so that

$$q_c \equiv \tau\dot{\epsilon}_c^{pl} = \sqrt{\tilde{\rho}} f_p(\sigma_c), \tag{25}$$

where $\tilde{\rho} = \frac{b^2\rho}{3}$, which is the dimensionless version of $\rho$, and $q_c$ is the dimensionless plastic strain rate[12,15], and

$$f_p(\sigma_c);= \exp\bigg( - \frac{T_p}{T} e^{-\sigma_c/\sigma_T} \bigg), \tag{26}$$

with

$$\sigma_T = \overline{\mu}_T \sqrt{\tilde{\rho}}, \tag{27}$$

where $\overline{\mu}_T = \sqrt{3}\mu_T$.

The dislocation density evolution equation follows from the second law of thermodynamics and the proportionality between the plastic work rate of deformation and the rate at which dislocations are formed[15]:

$$\dot{\rho} = \kappa_p \frac{\sigma_c \dot{\epsilon}_c^{pl}}{\gamma_D} \bigg[ 1 - \frac{\rho}{\rho^{ss}(\chi_c)} \bigg]. \tag{28}$$

Here, $\gamma_D$ is the dislocation energy per unit length and $\kappa_\rho$ is a dimensionless conversion factor for the fraction of energy inputs that is converted into dislocations. From[15], we know that $\rho^{ss}(\chi_c) = (1/a^2)e^{-e_D/\chi_c}$. The effective temperature evolution equation follows from the following equation (6):

$$c_c^{\text{eff}} \dot{\chi}_c = \sigma_c \dot{\epsilon}_c^{pl} \bigg( 1 - \frac{\chi_c}{\chi_0} \bigg). \tag{29}$$

According to the strain-hardening analysis presented in[14,15], $\kappa_\rho$ assumes the form

$$\kappa_\rho = \frac{\tilde{\kappa}_\rho}{\nu(T, \tilde{\rho}, q_c)^2}, \tag{30}$$

where $\tilde{\kappa}_\rho$ is of order unity. The quantity $\nu(T, \tilde{\rho}, q_c)$ is given by

$$\nu(T, \tilde{\rho}, q_c) = \frac{\sigma_c}{\overline{\mu}_T \sqrt{\tilde{\rho}}} = \ln\bigg( \frac{T_P}{T} \bigg) - \ln\bigg[ \ln\bigg( \frac{\sqrt{\tilde{\rho}}}{q_c} \bigg) \bigg]. \tag{31}$$

Combining equations (28), (30), and (31), the equation for the evolution of $\rho$ becomes

$$\dot{\rho} = \frac{\kappa_1 \sigma_c \dot{\epsilon}_c^{pl}}{\nu(T, \tilde{\rho}, q_c)^2 \overline{\mu}_T a^2} \bigg( 1 - \frac{\rho}{e^{-\beta/\chi_c}} \bigg), \tag{32}$$

where

$$\kappa_1 = \tilde{\kappa}_\rho \frac{a^2 \overline{\mu}_T}{\gamma_D}. \tag{33}$$

Here, $\kappa_1$ is of order unity and is related to the fraction of energy input stored in newly-formed dislocations.

## III. COUPLING THE AMORPHOUS AND CRYSTALLINE MATERIALS

Simulations and experimental data in[2–4,6] suggest that there is more plastic deformation associated with increased dislocation and STZ activity level near the interface. Furthermore, the data suggest that the interface mediates the conversion of dislocations into STZs. As such, we incorporate into the effective temperature evolution equations a conduction term to describe this interaction[1], which accounts for the flow of configurational disorder. The dislocation flux in this event can be described by

$$\bigg( \frac{d\chi}{dt} \bigg)_{\text{diff}} = D a^2 \dot{\epsilon}^{pl} \frac{\partial^2 \chi}{\partial y^2}, \tag{34}$$

where $D$ is the effective temperature diffusion constant and as before, $a$ is the atomic diameter, $\dot{\epsilon}^{pl}$ is the plastic strain rate, and $\chi$ is the effective temperature.

### A. Dimensionless form of the equations for uniaxial loading

It is both convenient and insightful to present the evolution equations in dimensionless form. To this end, we first replace time derivatives with derivatives with respect to the total strain $\epsilon$ at constant strain rate by applying the chain rule $\frac{d}{dt} = \frac{d}{d\epsilon}\frac{d\epsilon}{dt}$. We define the dimensionless plastic rate to be $q = \tau \dot{\epsilon}^{pl}$, for the respective layers, and $q_0 = \tau \dot{\epsilon}$.

For parallel loading, the two types of layers co-deform so that $\dot{\epsilon}_a = \dot{\epsilon}_c \equiv \dot{\epsilon}$. We also divide by Young's modulus such that $\tilde{\sigma}_a = \sigma_a/E_a$ and $\tilde{\sigma}_c = \sigma_c/E_c$, and rescale $\tilde{\mu}_T = \overline{\mu}_T/E_c$. Finally, $\tilde{\chi}$ is made dimensionless by rescaling with the STZ formation energy $e_Z$ and dislocation formation energy $e_D$ for the respective layers. Thus we arrive at the complete set of equations:

$$\frac{d\tilde{\sigma_a}}{d\epsilon} = 1 - \frac{1}{q_0 L_a} \int_0^{L_a} q_a(y) dy, \tag{35}$$

$$\frac{d\tilde{\chi_a}}{d\epsilon} = \frac{\kappa_a \tilde{\sigma}_a q_a}{q_0} \bigg( 1 - \frac{\tilde{\chi_a}}{\tilde{\chi_0}} \bigg) + \frac{D_a a^2 q_a}{q_0} \frac{\partial^2 \tilde{\chi_a}}{\partial y^2}, \tag{36}$$

$$\frac{d\tilde{\chi_c}}{d\epsilon} = \frac{\kappa_c \tilde{\sigma}_c q_c}{q_0 \tilde{\mu}_T} \bigg( 1 - \frac{\tilde{\chi_c}}{\tilde{\chi_0}} \bigg) + \frac{D_c a^2 q_c}{q_0} \frac{\partial^2 \tilde{\chi_c}}{\partial y^2}, \tag{37}$$

$$\frac{d\tilde{\rho}}{d\epsilon} = \frac{\kappa_1 q_c \tilde{\mu}_T \tilde{\rho}}{q_0 \tilde{\sigma}_c} \bigg( 1 - \frac{\tilde{\rho}}{e^{-\beta/\tilde{\chi_c}}} \bigg), \tag{38}$$

$$\frac{d\tilde{\sigma_c}}{d\epsilon} = 1 - \frac{1}{q_0 L_c} \int_0^{L_c} q_c(y) dy. \tag{39}$$

TABLE I. Table of thicknesses analyzed

| Sample Set | $L_a$ (nm) | $L_c$ (nm) | $L_a/L_c$ |
|---|---|---|---|
| A | 2.5, 5, 7.5 | 5 | 0.50, 1.00, 1.50 |
| B | 2.5 | 2.5,5,7.5,10 | 1.00, 0.50, 0.33, 0.25 |

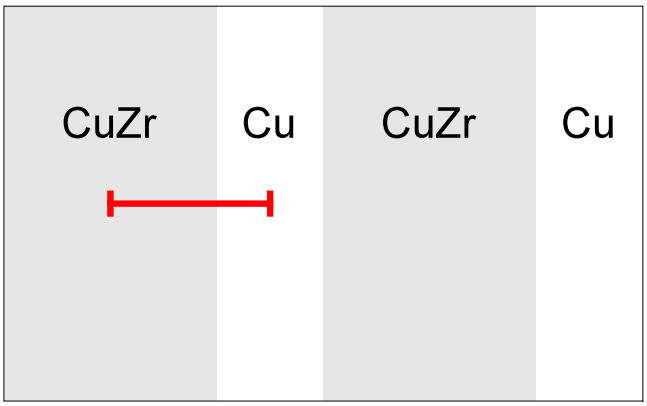


FIG. 1. Our domain for modeling the nanolaminate. Through symmetry and the assumption that interactions between the layers do not vary along the amorphous-crystalline interface (ACI), we can model from the midpoint of the amorphous layer to the midpoint of the crystalline layer

These expressions completely describe uniaxial tensile loading.

For perpendicular loading, the stress is uniform throughout the material and we cannot assume co-deformation. Thus we use for our stress variable $\tilde{\sigma}_a = \tilde{\sigma}$ and $\tilde{\sigma}_c = \frac{E_a}{E_c}\tilde{\sigma}$. We can determine $\tilde{\sigma}$ by taking the average total strain $\dot{\epsilon}$ and finding $\dot{\epsilon}_c$ and $\dot{\epsilon}_a$

$$\dot{\epsilon} = \frac{L_c\dot{\epsilon}_c + L_a\dot{\epsilon}_a}{L_c + L_a}. \tag{40}$$

By using Hooke's law for both layers, as in equations (11) and (17), and then eliminating $\dot{\epsilon}_a$ and $\dot{\epsilon}_c$ to get $\dot{\epsilon}$, we obtain

$$\frac{d\tilde{\sigma}}{d\epsilon} = \frac{Ec}{\frac{L_a}{L_c}E_c + E_a}\left[\left(\frac{L_a}{L_c}+1\right) - \frac{1}{q_0 L_c}\left(\int_0^{L_a} q_a(y)dy + \int_0^{L_c} q_c(y)dy\right)\right]. \tag{41}$$

The other evolution equations are

$$\frac{d\tilde{\chi_a}}{d\epsilon} = \frac{\kappa_a\tilde{\sigma}q_a}{q_0}\left(1 - \frac{\tilde{\chi_a}}{\tilde{\chi_0}}\right) + \frac{D_a a^2 q_a}{q_0}\frac{\partial^2\tilde{\chi_a}}{\partial y^2}, \tag{42}$$

$$\frac{d\tilde{\chi_c}}{d\epsilon} = \frac{\kappa_c E_a\tilde{\sigma}q_c}{E_c q_0\tilde{\mu_T}}\left(1 - \frac{\tilde{\chi_c}}{\tilde{\chi_0}}\right) + \frac{D_c a^2 q_c}{q_0}\frac{\partial^2\tilde{\chi_c}}{\partial y^2}, \tag{43}$$

$$\frac{d\tilde{\rho}}{d\epsilon} = \frac{\kappa_1 E_c\tilde{\mu_T}\tilde{\rho}}{E_a q_0\tilde{\sigma}}\left(1 - \frac{\tilde{\rho}}{e^{-\beta/\tilde{\chi_c}}}\right). \tag{44}$$

## IV. RESULTS

### A. Discretization

Fig. 1 shows the model domain for the amorphous/crystalline composite. The domain over which we solve the equations stretches from the middle of one layer to the middle of the next by virtue of symmetry. The half-layer thicknesses (Fig. 1) are designated as $L_a$ and $L_c$. The domain is discretized into grid points, where $N_a$ and $N_c$ are the number of grid points in the amorphous and crystalline layer respectively. These points are finely spaced by $\Delta y = 5$Å. Thus, the entire domain contains $N_a + N_c$ grid points, with $N_a = L_a/\Delta y$ and $N_c = L_c/\Delta y$. The particular layer thicknesses we study here are given in Table I.

Using an adaptive time-stepping scheme, we obtain a finer time resolution near yielding, when the stress changes dramatically, without incurring longer calculation run times as we approach the steady state.

### B. Parameter characterization

To characterize the material parameters introduced in the formulation, we fit the parameters by comparing simulation data from tensile deformation of nanocrystalline (polycrystalline) Cu alone to experimental tests provided in the literature. For the amorphous material, the parameters are selected so that the two-phase amorphous/crystalline model qualitatively provides trends reported in the literature for tensile parallel to the amorphous-crystalline interface (ACI).

The values of parameters for the nanocrystalline layer, namely $\kappa_1$, $\rho(0)$, and $\chi_c(0)$, are determined by comparing the stress versus strain curves from the MD simulations for pure Cu tensile deformation[2] to the curves obtained from the effective-temperature theory applied on Cu alone. Fig. 2 shows the comparison for an imposed strain rate of $10^8$ s$^{-1}$[2].

Cheng and Trelewicz[2] performed MD simulations of the amorphous CuZr and nanocrystalline (polycrystalline) Cu composite loaded under uniaxial tension parallel to the interfacial direction, and measured the slip strain profiles and stress-strain behavior. To characterize the material parameters for the amorphous layer and the diffusion constants, namely $D_a$, $D_c$, $\epsilon_0$, $\epsilon_Z$, and $\chi_a(0)$, we compare the nanolaminate results from the effective-temperature theory to the simulations with varied thicknesses according to Table I[3]. In this case, we exploit that fact that it is known that increasing the amorphous layer

TABLE II. Table of parameter values. The asterisk (*) indicates tunable parameters that we adjusted.

| Variable | Description | Value |
|---|---|---|
| $\tilde{\chi}_0$* | Steady-state effective temperature | 0.04 |
| $T$ | Thermal temperature | 298K |
| $E_a$ | Young's modulus | 72GPa |
| $E_c$ | Young's modulus | 110GPa |
| $\tau$ | Atomic time scale | $10^{-12}$ s |
| $T_P$ | Depinning energy | 40800K |
| $\kappa_1$* | Conversion factor | 185 |
| $\kappa_c$* | Conversion factor | 11 |
| $\kappa_a$* | Conversion factor | 80 |
| $\epsilon_0$* | STZ core volume in units of $a^3$ | 4 |
| $\tilde{\epsilon}_Z$* | Rescaled STZ formation energy | 0.195 |
| $\beta$ | Dislocation-STZ energy ratio | 0.16 |
| $D_a$* | Diffusion constant | 10000 |
| $D_c$* | Diffusion constant | 1.5 |
| $a$ | Atomic size | 0.167nm |
| $\overline{\mu}_T$* | Rescaled depinning reference stress | 6.5GPa |
| $\tilde{\sigma}_a(0)$ | Initial dimensionless stress | $10^{-5}$ |
| $\tilde{\sigma}_c(0)$ | Initial dimensionless stress | $10^{-5}$ |
| $\tilde{\chi}_a(0)$* | Initial dimensionless effective temperature | 0.025 |
| $\tilde{\chi}_c(0)$* | Initial dimensionless effective temperature | 0.040 |
| $\tilde{\rho}(0)$* | Initial dimensionless dislocation density | 0.002 |

thickness gives rise to a greater maximum flow stress (Fig. 3). A higher yield strength for greater CuZr thicknesses can be attributed to their lack of atomic crystalline order[16].

As mentioned in the development of the formulation, $\sigma_0$ emerges as an important parameter. Based on experimental results for stress versus strain curves for single-phase pure Cu[11], $\sigma_0$ is around 0.02 times the Young's modulus $E_a$ except near the interface; we use

$$\frac{\sigma_0(x)}{E_a} = 0.02 - 0.0001e^{6-x}, \tag{45}$$

where $x$ is the position from the interface in nanometers. $\sigma_0$, as chosen according to Eq. (45), is smaller near the amorphous-crystalline interface. This choice is further validated from the expression for the strain rate, Eq. (12) along with Eq. (16), which is necessary to account for the increased slip activity observed near the interface compared to further in the amorphous layer. This, in turn, suggests that the amorphous material is weaker there[2]. The exponential in Eq. (45) ensures that $\sigma_0$ is bounded and does not depend on interfacial physics at positions far from the interface. The remaining parameters used in the present simulations can be found in[1]. All other parameters are listed in Table II.

As a final verification of the parameters, we compare in Fig. 4 the slip strain from[2] to our slip strain results at different levels of applied strain in tension. Here we borrow the same definition of slip distance $S$, namely

$$S = d\int_0^t dt' \dot{\epsilon}_a^{pl}(t'), \tag{46}$$

where $d = 6.5$Å is a microscopic length scale determined by direct parameter fitting. As shown in Fig. 4, the agreement between theory and simulation from[2] is reasonable indicating that the model parameters are reliable for further use in extrapolating to other loading configurations. There are, however, some discrepancies. We slightly underestimated the slip distance in the crystalline Cu layer at the early stages of strain hardening and, in the absence of finer resolution in the data for slip distance, were only able to provide an estimate of the slip strain deep inside the amorphous CuZr.

### C. Results for compressive loading perpendicular to the interface

From the parameter values we deduced from comparing the simulation data in[2,3], we predict the material response under uniaxial compression perpendicular to the interfaces.

For perpendicular compression, peak flow stress increases as the amorphous-to-crystalline layer thickness ratio $L_a/L_c$ increases, as in the case of tensile loading parallel to the interfaces. (Figs.6 and 7).

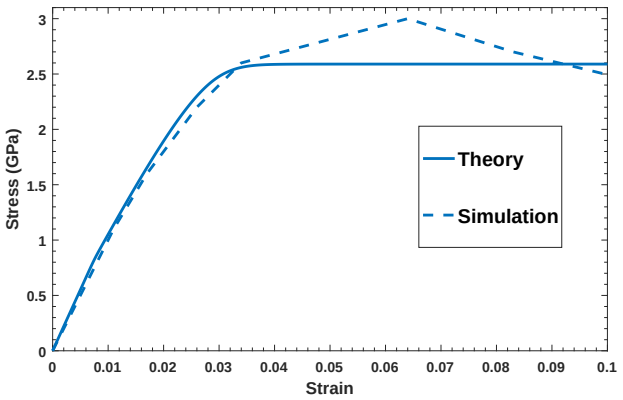


FIG. 2. Parallel loading stress versus strain curve from the effective-temperature theory in Cu plotted over the Cheng (2016) result for Cu for an imposed strain rate of $\dot{\epsilon} = 10^8$ s$^{-1}$. The quantities $\kappa_1$, $\rho(0)$, and $\chi_c(0)$ are constrained through this comparison.

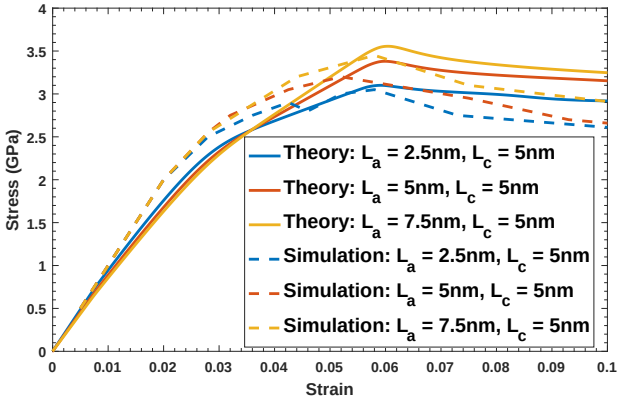


FIG. 3. Parallel loading stress versus strain curve for sample set A (solid) plotted over the Cheng (2018) result (dashed) for thickness variations and an imposed strain rate of $\dot{\epsilon} = 10^8$ s$^{-1}$. Increasing the thickness in the amorphous layer increases the maximum flow stress. The parameters $D_a$, $D_c$, $\epsilon_0$, $\epsilon_Z$, and $\chi_a(0)$ are constrained through this comparison.

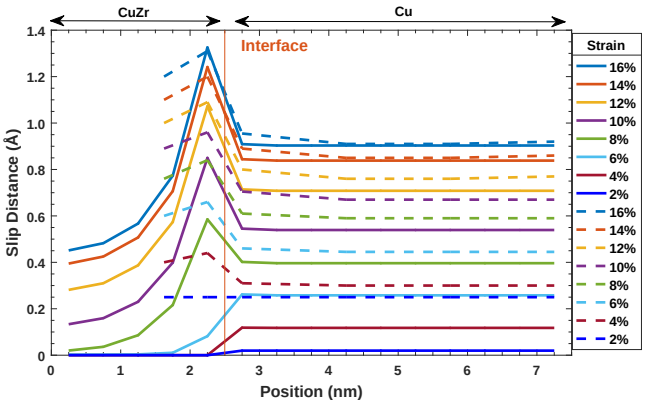


FIG. 4. Parallel loading slip profile from the effective-temperature theory (solid) plotted over simulation data (dashed) for an imposed strain rate of $\dot{\epsilon} = 10^8$ s$^{-1}$. The maximum slip lies in the amorphous layer for both theory and simulation results suggesting that the nanolaminate's plastic flow is Cu dominated. This slip profile further validates our parameter values constrained from the stress versus strain comparisons. MD simulation results are taken from[2]

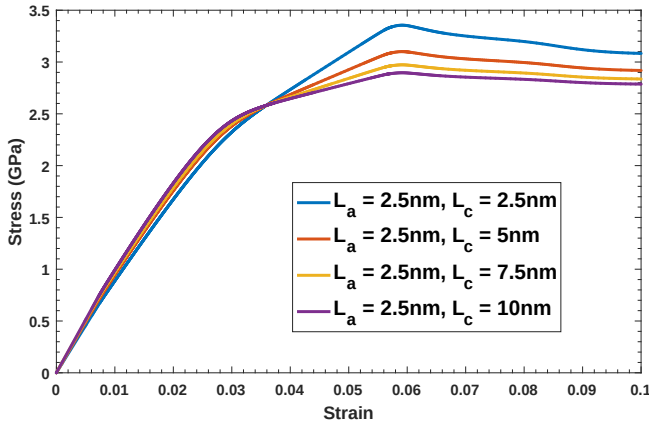


FIG. 5. Parallel loading stress versus strain curve for sample set B and an imposed strain rate of $\dot{\epsilon} = 10^8$ s$^{-1}$. Similarly to sample set A, we find that increasing the $L_a/L_c$ ratio increases the maximum yield strength, further validating our parameter values.

Next, we use the parameters listed in Table II to predict the effect of layer thickness and strain rate on the spatial distribution of slip across the layers and the flow stress for uniaxial compression perpendicular to the ACI. At all accumulated strains, almost all of the slip is accumulated in the crystalline Cu as opposed to the amorphous CuZr (Fig. 8), increasing nearly linearly with the total strain. This is in stark contrast to the observation under tensile loading parallel to the interfaces (Fig. 4), in which case the maximum slip strain is observed in the amorphous CuZr immediately adjacent to the interface. This anisotropy is interesting and may have important practical implications in the design and fabrication of mechanical metamaterials that absorb shock and are damage-resistant in some directions but not others.

### D. Layer thickness dependence for parallel loading

Our analyses thus far indicate that increasing the $L_a$ / $L_c$ ratio results in greater maximum flow stress (Figs. 3 and 5), for both tensile loading parallel to, and compression perpedicular to, the Cu/CuZr interfaces, for fixed $L_a$ or $L_c$. We now allow $L_a$ and $L_c$ to change concomitantly and study how changing the layer thickness while keeping the $L_a/L_c$ ratio fixed alters the response to parallel loading.

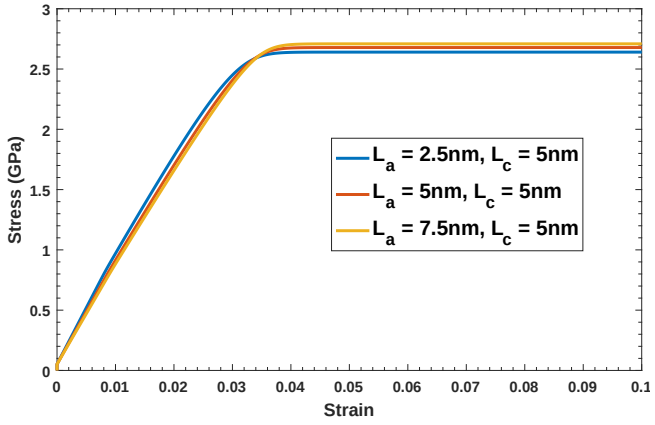


FIG. 6. Sample set A stress versus strain curve for perpendicular loading and an imposed strain rate of $\dot{\epsilon} = 10^8$ s$^{-1}$. We constrained our parameters with experimental results in parallel loading. The onset of plasticity is at a strain of around 0.02 and the ultimate strength is around 2.6 GPa. Also, an increased amorphous-to-crystalline layer thickness ratio gives rise to greater maximum flow stress similar to the case of parallel loading.

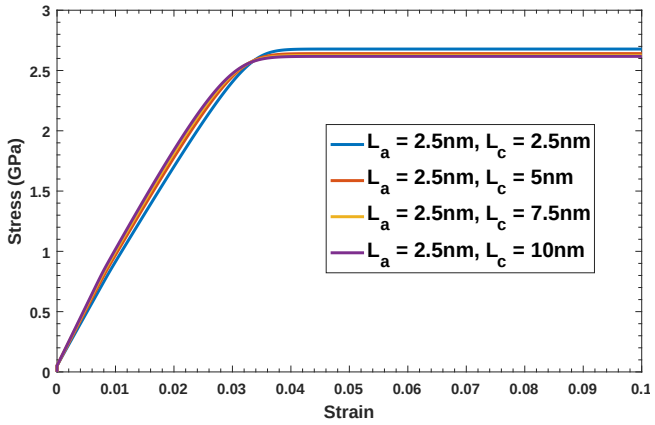


FIG. 7. Sample set B stress versus strain curve for perpendicular loading and an imposed strain rate of $\dot{\epsilon} = 10^8$ s$^{-1}$ that is compatible with the observation that greater amorphous layer thickness gives rise to greater flow stress. The onset of plasticity is around a strain of 0.02 and the ultimate strength is around 2.6 GPa.

In Fig. 9, the two stress versus strain curves are nearly identical despite the absolute thicknesses varied by a factor of 2. Yet in Fig. 10, we find that increasing the strain for $L_a = 5$nm and $L_c = 10$nm increases the overall slip strain in the amorphous layer more than the case for $L_a = 2.5$nm and $L_c = 5$nm. This increase is most prominent near the interface, where the maximum slip distance for $L_a = 2.5$nm and $L_c = 5$nm is around 1.3 Å, whereas for $L_a = 5$nm and $L_c = 10$nm it is around 2.0 Å. This implies that the overall slip profile in the amorphous layer

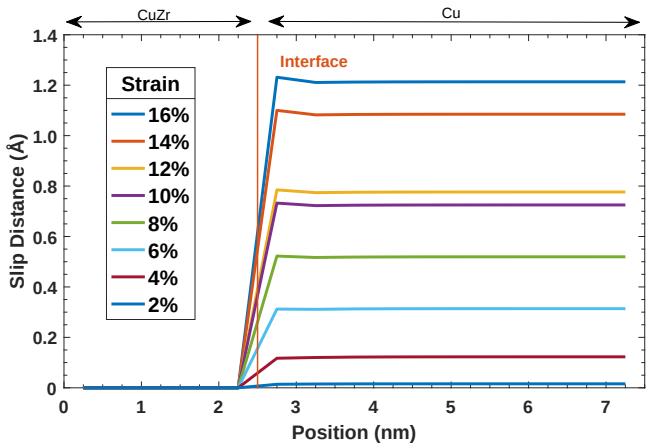


FIG. 8. Slip profile prediction based from the effective-temperature theory applied to perpendicular loading for an imposed strain rate of $\dot{\epsilon} = 10^8$ s$^{-1}$. Most of the slip accumulates in Cu because this layer is weaker than the amorphous layer in terms of flow stress.

is affected more strongly by absolute thickness than the maximum flow stress, which is affected more strongly by thickness ratio.

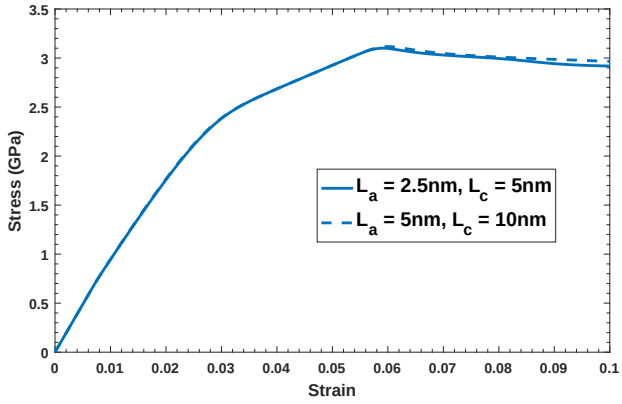


FIG. 9. Parallel loading stress versus strain curves for an imposed strain rate of $\dot{\epsilon} = 10^8$ s$^{-1}$. The curves are nearly identical despite the amorphous and crystalline layer thicknesses doubling with maximum flow stress at 3.2 GPa.

Fig. 11 demonstrates the effects of amorphous layer size on the calculated slip profile for 16 % strain in the case of parallel loading, using the same cases as sample set A. Increasing the amorphous layer thickness increases the maximum slip in the amorphous CuZr, while increasing the slip strain in the crystalline Cu only very slightly. We speculate that this size effect is associated with an increase in the capacity for the amorphous layer to act as a dislocation sink[17].

Likewise in Fig. 12, we show the effects of crystalline layer size for sample set B at $L_a = 2.5$nm, $L_c = 2.5$nm (Fig. 5). Here we observe that the greatest slip dis-

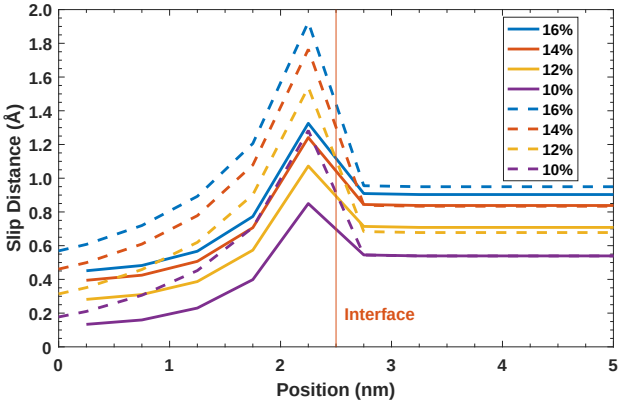


FIG. 10. Parallel loading slip profile for $L_a = 2.5$nm, $L_c = 5$nm (solid lines) against $L_a = 5$nm, $L_c = 10$nm (dashed lines) for an imposed strain rate of $\dot{\epsilon} = 10^8$ s$^{-1}$. Doubling the layers thicknesses increases the maximum slip strain in the CuZr layer. Note that the position in the slip profile for $L_a = 5$nm, $L_c = 10$nm is translated by 2.5nm to the left.

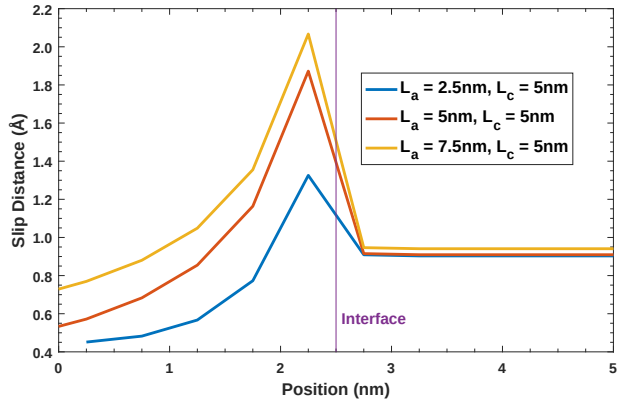


FIG. 11. Parallel loading slip profile for 16% strain with varied thicknesses according to sample set A for an imposed strain rate of $\dot{\epsilon} = 10^8$ s$^{-1}$. Increasing the amorphous layer thickness increases the maximum slip in the amorphous and crystalline layers. Note that for $L_a = 5$nm, $L_c = 5$nm, the slip profile is translated 2.5nm to the left and for $L_a = 7.5$nm, $L_c = 5$nm, the slip profile is translated 5nm to the left.

tance occurs at the same thickness values as the maximum stress. Generally, overall slip increases with a greater $L_a/L_c$ ratio except when increasing $L_c$ from 5nm to 7.5nm.

Taken together, between slip profiles for set A and B (Fig. 11 and 12), we see that increasing the amorphous layer thickness does not affect slip in the crystalline layer. However, increasing the crystalline layer thickness adjusts slip throughout the entire nanolaminate, further suggesting that plasticity for an imposed strain rate of $10^8$ s$^{-1}$ is dominated by Cu. Furthermore, the maximum slip strain corresponds with highest $L_a$ / $L_c$ ratio values.

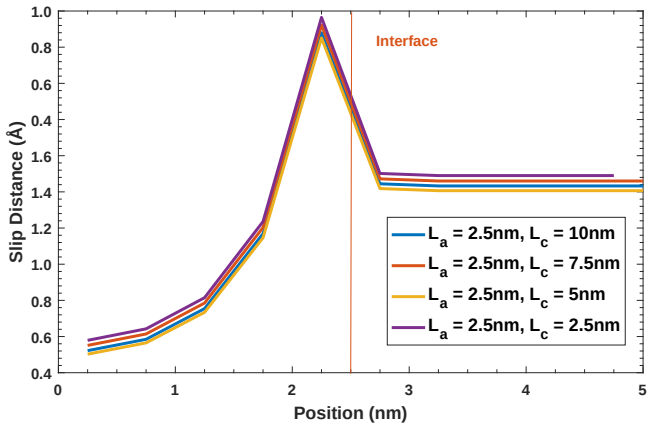


FIG. 12. Parallel loading slip profile for 16% strain with varied thicknesses according to sample set B and for an imposed strain rate of $\dot{\epsilon} = 10^8$ s$^{-1}$. The thicknesses associated with the greatest slip strain is $L_a = 2.5$nm, $L_c = 2.5$nm. Generally, the slip distance decreases as the crystalline layer increases except between $L_c = 5$nm to $L_c = 7.5$nm.

### E. Layer thickness dependence for perpendicular loading

Similar to the parallel loading case, an increase in $L_a/L_c$ gives rise to an increase in maximum flow stress (Fig. 6 and 7). Yet, as demonstrated in Fig. 13, a change in the absolute thickness values while keeping $L_a/L_c$ fixed, say if $L_a$ and $L_c$ are doubled, does not alter the flow stress versus strain response. Similarly, as shown in Fig. 14, doubling $L_a$ and $L_c$ does not alter the slip strain profile near the interface. These results would indicate that the slip profile is controlled by the relative layer thickness rather than absolute layer thickness for the perpendicular loading case. From Figs. 9 and 10, we may conclude that the ratio of layer thicknesses affects the maximum flow stress and slip distance much more than the absolute thickness does.

As in the case of parallel loading, at 16% strain, an increase in $L_a/L_c$ ratio values gives rise to an increase in maximum slip strain with the maximum in the amorphous layer (Figs. 9 and 10). However, for perpendicular deformation at $10^8$ s$^{-1}$, most of the slip strain is in the crystalline layer (Fig. 15 and 16). Also for both parallel and perpendicular loading, decreasing the layer thickness ratio by increasing the crystalline layer while keeping $L_a$ fixed generally decreases overall slip distance except between an increase from $L_c = 5$nm and $L_c = 7.5$nm.

The slip strain in the amorphous layer layer is minimal because the amorphous layer is stronger than the crystalline layer, as seen from Figs. 6 and 7 for an imposed strain rate of $10^8$ s$^{-1}$ under perpendicular loading.

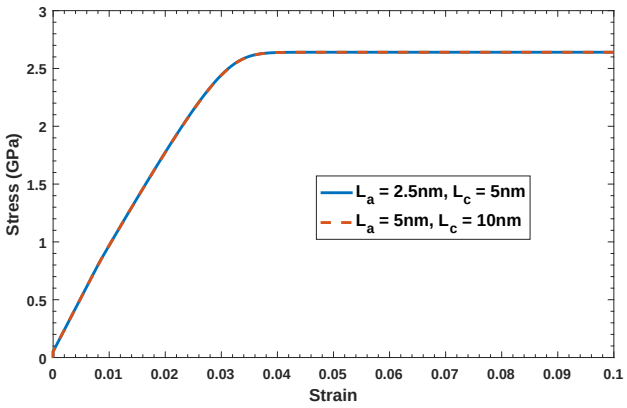


FIG. 13. Perpendicular loading stress versus strain curves for an imposed strain rate of $\dot{\epsilon} = 10^8$ s$^{-1}$. The curves are identical despite the amorphous and crystalline layer thicknesses doubling.

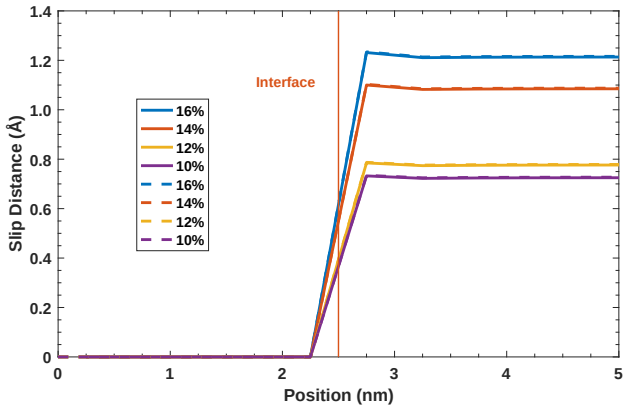


FIG. 14. Perpendicular loading slip profile for $L_a = 2.5$nm, $L_c = 5$nm (solid) against $L_a = 5$nm, $L_c = 10$nm (dashed) for an imposed strain rate of $\dot{\epsilon} = 10^8$ s$^{-1}$. Doubling the layers thicknesses does not affect the overall slip strain for the nanolaminate.

### F. Strain rate dependence for tensile deformation parallel to the interface

Next we investigate the effect of strain rate on the deformation behavior of the nanolaminate. We study a broad range of strain rates, from $10^{-3}$ s$^{-1}$ through $10^8$ s$^{-1}$. This range encompasses strain rates used in laboratory tests as well as rates employed in MD simulations. Figure 17 presents flow stress results from the theory at different rates in parallel loading. As can be seen, the maximum flow stress occurs at increasing strain values for higher imposed strain rates. At an imposed strain rate of $10^8$ s$^{-1}$, we find that the maximum flow stress is around 3.2 GPa, whereas lowering the imposed strain rate lowers the maximum flow stress.

For imposed strain rates 10 s$^{-1}$ through $10^3$ s$^{-1}$, we find that increasing the imposed strain rate has little effect on the slip strain in Cu near the interface, but significantly decreases the slip strain near the interface in CuZr (Fig. 18).

At lower strain rates, the plastic response of the nanolaminate is dominated by Cu because of the stress threshold $\sigma_0$ for flow in the amorphous layer, implying that the onset of plasticity takes longer in the amorphous layer. The decrease in slip strain near the interface in Cu, as the imposed loading rate increases, suggests that this domination by Cu is most prominent at an imposed strain rate of 10 s$^{-1}$. As the imposed strain rate increases from $10^4$ s$^{-1}$ to $10^8$ s$^{-1}$, the domination of Cu over CuZr di-

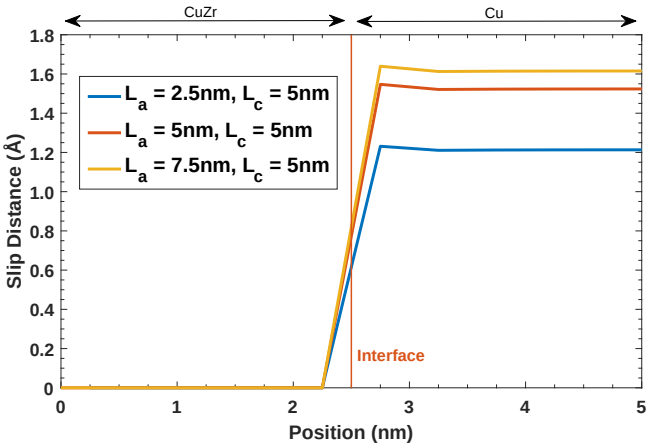


FIG. 15. Perpendicular loading slip profile for 16% strain with varied thicknesses according to sample set A and for an imposed strain rate of $\dot{\epsilon} = 10^8$ s$^{-1}$. Increasing the amorphous layer thickness increases the maximum slip. The slip in the amorphous layer is minimal because it is stronger than the crystalline layer.

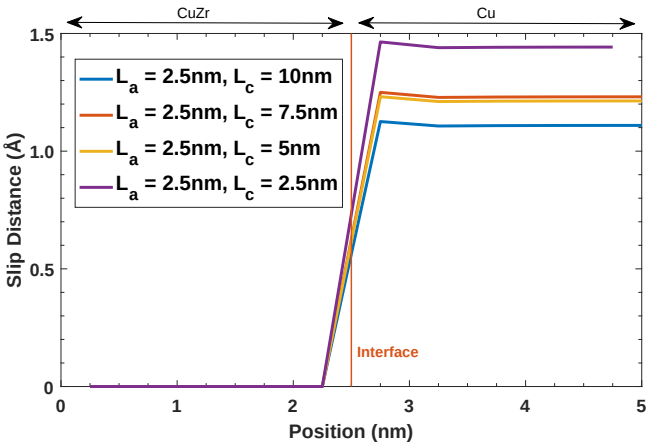


FIG. 16. Perpendicular loading slip profile for 16% strain with varied thicknesses according to sample set B and for an imposed strain rate of $\dot{\epsilon} = 10^8$ s$^{-1}$. The thicknesses associated with the greatest slip strain is $L_a = 2.5$nm, $L_c = 2.5$nm. However, decreasing the layer thickness ratio by increasing the crystalline layer thickness generally decreases the slip distance except between $L_c = 5$nm to $L_c = 7.5$nm.

minishes, as evidenced by the increase of slip strain deep in the CuZr.

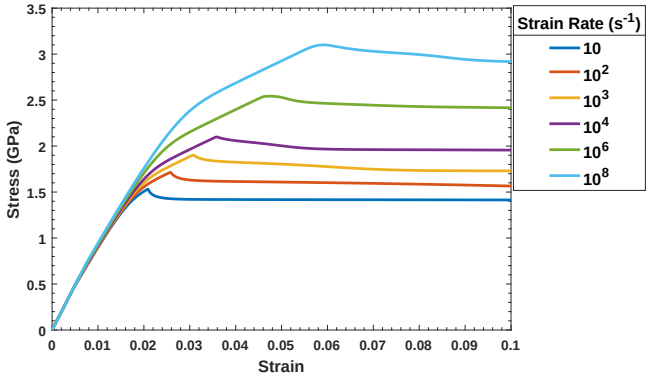


FIG. 17. Parallel loading stress versus strain for varied imposed strain rates and $L_a = 2.5$nm, $L_c = 5$nm. As the strain rate increases, the maximum flow stress increases up to around 3.2 GPa at $10^8$ s$^{-1}$.

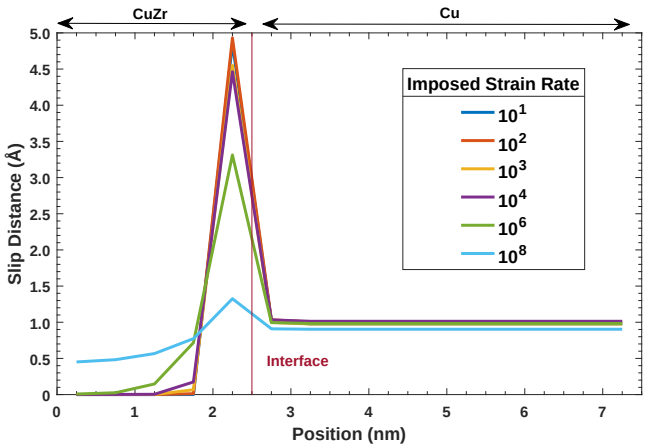


FIG. 18. Parallel loading slip profile for 16% strain and $L_a = 2.5$nm, $L_c = 5$nm with varied imposed strain rates. For imposed strain rates 10 s$^{-1}$ through $10^3$ s$^{-1}$, the nanolaminate's plasticity is Cu dominant. At around an imposed strain rate of $10^8$ s$^{-1}$, the nanolaminate's plasticity begins to shift to CuZr dominant.

### G. Strain rate dependence for compressive deformation perpendicular to the interface

Figure 19 presents the flow stress computed at different rates for compressive deformation perpendicular to the interface. In this case, we observe that the maximum flow stress for each imposed strain rate occurs around a strain of 0.02. Also, higher imposed strain rates result in higher maximum flow stresses. At an imposed strain rate of $10^8$ s$^{-1}$, the maximum flow stress is around 2.6 GPa (Fig. 19). Up to a strain rate of $10^2$ s$^{-1}$, the slip profile has a peak in the amorphous CuZr adjacent to the interface, while there is little plastic deformation in the crystalline Cu (Fig. 20). At loading rates of $10^3$ s$^{-1}$ and above, however, the slip profile peak in amorphous CuZr disappears. The crystalline Cu, which absorbs much of the plastic deformation, shields the amorphous CuZr from plastic flow.

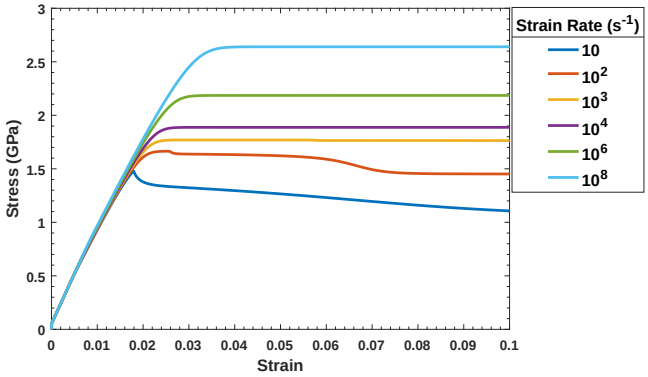


FIG. 19. Perpendicular loading stress versus strain for varied imposed strain rates and $L_a = 2.5$nm, $L_c = 5$nm. As the strain rate increases, the maximum flow stress increases up to around 2.6 GPa at $10^8$ s$^{-1}$.

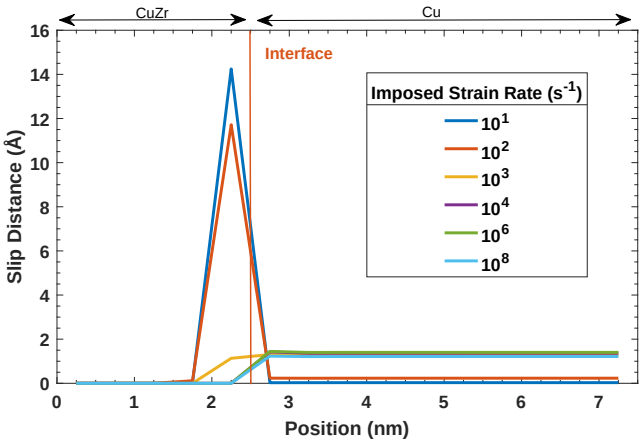


FIG. 20. Perpendicular loading slip profile for 16% strain and $L_a = 2.5$nm, $L_c = 5$nm with varied imposed strain rates. Increasing the strain rate decreases the domination of Cu plasticity, and at $10^3$ s$^{-1}$, plasticity in the nanolaminate is dominated by CuZr.

## V. SUMMARY AND CONCLUDING REMARKS

In this paper, we present a modeling framework for deformation in amorphous-crystalline nanolaminates. It combines the effective-temperature models for dislocation plasticity in polycrystalline materials and shear-transformation-zone plasticity in amorphous materials, both of which are based upon the idea that the defect

density in a material is controlled by its state of configurational disorder. In addition, the model provides a straightforward tool to describe the interface-mediated interaction between STZs on the amorphous side and dislocations on the nanocrystalline side, and explicitly represents the increased rate of STZ activity near the interface via a position-dependent yield stress parameter $\sigma_0$ which is inversely proportional to the rate of STZ formation and annihilation.

A direct implementation of the simplified, one-dimensional version of the framework closely reproduces the stress-strain behavior and cross-sectional slip profiles observed in MD simulations[3] of the Cu/CuZr nanolaminate structure undergoing tensile deformation parallel to the interfaces, and reveals system parameter values indicative of a lower resistance to plastic flow in the nanocrystalline Cu layers than in amorphous CuZr. These parameters are then used to provide predictions for the stress-strain behavior of the Cu/CuZr nanolaminate material at various loading rates, as well as for uniaxial compressive loading perpendicular to the Cu/CuZr interfaces, which can be verified by simulations and experiments, such as micropillar compression tests.

Despite the small thickness of the nanocrystalline Cu layers, a dislocation-density representation and the isotropic Orowan equation for the plastic strain rate are still appropriate and of practical utility for the present set-up. First of all, the thickness of the Cu, on the order of 5 nm, is roughly several dozen atomic diameters, and exceeds the minimum separation between dislocation lines; the dislocation density $\rho$ remains a meaningful quantity at this length scale. Secondly, this is a simplified one-dimensional model; we are in effect averaging over many cross sections perpendicular to the amorphous-crystalline interfaces, so the statistical concept of mean-field coarse-graining in our representation of dislocations do apply with useful validity. Finally, the simulation set-up contains *nanocrystalline* grains whose orientation varies from one grain to the next. In the absence of heavy textures, an isotropic plasticity description, which describes dislocation motion primarily through thermally-activated depinning of dislocations, suffices. Grain orientation is averaged over many grains, and it is largely unnecessary to capture slip system activation within the dislocation depinning model.

Crucially, the model reveals the anisotropy of mechanical response of the nanolaminate structure, which should not come as a surprise because of the different strengths and deformation mechanisms of nanocrystalline Cu versus amorphous CuZr. In particular, we predict that when compressed perpendicular to the interfaces at a strain rate of $10^3$ $s^{-1}$ or above, the nanocrystalline Cu absorbs practically all of the plastic deformation, leaving the amorphous CuZr largely undamaged. This stands in contrast to the case of loading parallel to the interfaces, in which the amorphous CuZr immediately adjacent to the Cu/CuZr interfaces experiences the greatest amount of slip. This anisotropy may be useful for designing next-generation energy and memory storage devices in which the need for mechanical insulation becomes a prime concern.

We conclude by calling for further experiments and simulations that reveal rate and anisotropy effects and may verify the model predictions made here. Such experiments and simulations may in addition reveal important new physics that would enrich the modeling framework.


[1] C. K. C. Lieou, J. Mayeur, and I. J. Beyerlein, *Modelling and Simulation in Materials Science and Engineering*, Modelling and Simulation in Materials Science and Engineering **5**, 034002 (2016).

[2] B. Cheng and J. R. Trelewicz, Acta Materialia **117**, 293 (2016).

[3] B. Cheng and J. R. Trelewicz, Acta Materialia **153**, 314 (2018).

[4] Y. Wang, J. Li, A. V. Hamza, and T. W. Barbee, Proceedings of the National Academy of Sciences **104**, 11155 (2007), http://www.pnas.org/content/104/27/11155.full.pdf.

[5] B. Arman, C. Brandl, S. N. Luo, T. C. Germann, A. Misra, and T. Cagin, Journal of Applied Physics **110**, 043539 (2011), https://doi.org/10.1063/1.3627163.

[6] J.-Y. Kim, D. Jang, and J. R. Greer, Advanced Functional Materials **21**, 4550 (2011), https://onlinelibrary.wiley.com/doi/pdf/10.1002/adfm.201101164.

[7] W. Guo, E. Jgle, J. Yao, V. Maier, S. Korte-Kerzel, J. M. Schneider, and D. Raabe, Acta Materialia **80**, 94 (2014).

[8] M. Liu, J. Huang, Y. Fong, S. Ju, X. Du, H. Pei, and T. Nieh, Acta Materialia **61**, 3304 (2013).

[9] J. Zhang, G. Liu, and J. Sun, *Scientific reports*, **3**, 2324 (2013).

[10] S. Shahrezaei, D. C. Hofmann, and S. N. Mathaudhu, JOM **71**, 585 (2019).

[11] E. Bouchbinder and J. S. Langer, Phys. Rev. E **80**, 031131 (2009).

[12] J. S. Langer, Phys. Rev. E **77**, 021502 (2008).

[13] M. L. Falk and J. Langer, Annual Review of Condensed Matter Physics **2**, 353 (2011), https://doi.org/10.1146/annurev-conmatphys-062910-140452.

[14] J. Langer, E. Bouchbinder, and T. Lookman, Acta Materialia **58**, 3718 (2010).

[15] J. S. Langer, Phys. Rev. E **92**, 012318 (2015).

[16] E. G. Daub, D. Klaumünzer, and J. F. Löffler, Phys. Rev. E **90**, 062405 (2014).

[17] J. Zhang, X. Zhang, R. Wang, S. Lei, P. Zhang, J. Niu, G. Liu, G. Zhang, and J. Sun, Acta Materialia **59**, 7368 (2011).